Proceedings World Geothermal Congress 2020+1
Reykjavik, Iceland, April - October 2021

Focused Geophysical Imaging of the Chiweta Geothermal Field (Malawi)

Egidio Armadillo[1], Daniele Rizzello[2], Riccardo Balsotti[3], Claudio Pasqua[3], Paolo Pisani[3], Biagio Giorgio[3], Eliyasi Charleson[4], Taramaeli Mnjokava[5], Jonas Mwano[5], Didas Makoye[5], Lucas Tumbu[5]

1) DISTAV, University of Genoa, Italy 2) Tellus s.a.s., Italy 3) ELC-Electroconsult s.p.a, Italy 4) Ministry of Natural Resources, Energy and Mining, Malawi 5) Tanzania Geothermal Development Company Ltd (TGDC), Tanzania

egidio.armadillo@unige.it

Keywords: Chiweta, gravity, magnetotellurics, inversion, imaging

ABSTRACT

Geophysical surveys may image buried tectonic structures and variations of lithology, hydrothermal alteration and porosity/fluid content of geothermal fields and inverse models can be directly used for the assessment of the conceptual models. However, conventional interpretation is commonly based on minimum-structure inverse modelling that produces inherently smooth and blurred images of the investigated geological structures. Therefore, while smooth modelling helps inversion convergence and prevent artefacts in the solutions, some important features with sharp transitions can be missed or smoothed out. Typical examples are the lithological variations between the sedimentary infill and the bedrock in a basin or the bedrock steps due to faulting in graben/horst structures.

Focused geophysical imaging with different regularization methods can be more effective to detect sharp boundaries because they don't excessively penalize sharp physical property variations. We have applied the modified total variation (MTV) and the minimum gradient support (MGS) stabilizers to the inversion of gravimetric data collected at the Chiweta geothermal prospect in Malawi and compared them to the electrical resistivity models from magnetotellurics.

The gravimetric data have been used to map the interface between the Karoo sandstones and the underlying Precambrian gneiss basement complex, assuming a density contrast of 200 kg/m^3 between the two formations. The resulting horst-graben structure imaged by the 2D and 3D MGS inversion allows to identify major faults affecting the basement and possibly driving the up-flow of hydrothermal fluids.

Electrical resistivity models from magnetotelluric show the lithological contact between the Karoo sandstones and the basement complex in the central portion of the survey area. Geothermal alteration in the Karoo sandstones has been revealed by different conductive anomalies. Some of them are associated with low temperature clay alteration in the Chiweta hot springs area, while others may represent fossil geothermal zones. Good correspondence between higher density and resistivity values has been observed where geothermal alteration is plausibly weaker or absent.

It was found that focused inversion is strongly dependent upon the initial model and the chosen inversion parameters, but if a proper choice is done, it can be an effective tool to get detailed geological images. It was concluded that it can be considered as a refinement of the classical maximum smoothness approach, to be used when abrupt physical property changes are expected.

1. INTRODUCTION

Geophysical surveys are considered indispensable tools in geothermal exploration to image buried tectonic structures and variations of lithology, hydrothermal alteration type and porosity/fluid content. The final geophysical products are inverse models that can be directly used for the assessment of the geothermal conceptual model. Typical inverse models use Tikhonov (Tikhonov and Arsenin, 1977) zero order (minimum norm of the solution) or first order (minimum norm of the solution first derivative) regularization techniques (e.g. Zhdanov, 2002). While this approach prevents over-interpretation of the data, in some cases important abrupt changes of the geophysical parameters may be smoothed out and missed. Typical examples are the lithological variations between the sedimentary infill and the bedrock in a basin or the bedrock steps due to faulting in graben/horst structures.

Focused geophysical imaging can be effective to detect sharp boundaries allowing to map buried faulting in the bedrock and lithological variations. For instance, the total variation regularization function (Rudin et al., 1992) and its modifications (Vogel and Oman, 1998) can be effective when moderate discontinuous jumps in the model are expected. Another alternative is the minimum gradient support functional (Portniaguine and Zhdanov, 1999) that minimizes the area where strong model parameter variations and discontinuity occur and therefore helps to generate a stable solution of the inverse problem for complex geological environment that are better modelled by blocky rather than smooth structures.

We have applied these focused regularization techniques to the gravimetric data set collected over the geothermal field of Chiweta (Fig. 1), in Malawi, and compared the results to the electrical resistivity models derived from 3D smooth inversion of magnetotelluric data.

The Chiweta manifestations (Fig. 1) extend close to Lake Malawi within a small plane, about 500 m wide and 3 km long, oriented in a NW-SE direction. This flat area is bounded to the north by the Chiweta fault and to the west by an important NNE-SSW trending fault and is surrounded by mountains and hills characterized by rough morphology, rising to as much as 1,500 m a.s.l. The maximum outlet temperature is about 80°C and the flow rate is higher than 30 L/s.

The hot springs of Chiweta have a small oxygen isotope shift, ≤0.4‰ units, distinguishing Chiweta from all the other thermal sites of Malawi. The oxygen isotope shift is likely due to water-rock interaction at relatively high temperature. As pointed out by the log(Q/K) vs. temperature plots for the samples least affected by secondary processes, the saturation temperature with several hydrothermal minerals indicates reservoir temperatures between 130 and 140°C. Due to the shift in oxygen isotopes, only the δ2H values can be used to evaluate the average infiltration elevation of the meteoric waters recharging the Chiweta system. They indicate an average recharge elevation of 1049±11 m a.s.l.

The stratigraphic setting of the Chiweta prospect (Fig. 1) is characterized by the presence of a wide NW-SE trending basin, which has been filled by products of the Karoo System. These products can reach a thickness of the order of 1,000 m and overlie the Basement Complex outcropping in the southwestern sector of the prospect. Chemistry of thermal water suggests its extensive interaction with the Karoo sedimentary rocks.

The rocks of the Basement Complex exhibit on the whole a moderate to good permeability, due to their gneiss banding, coarse grained crystals and microfractures between the grains, as well as the widespread presence of fracturing enhanced by neo-tectonic events. Permeability of the Karoo System, on the other side, is low to high, in consideration of the extreme variability of the products.

The structure of the prospect is dominated by the presence of major NW-SE trending faults, which extend for tens of kilometers and control the formation of the basin filled by the Karoo products, together with the transversal NE-SW system, which delimit the basin to the north-west. This structural setting favors the deep circulation of the waters, which tend to infiltrate in the highlands and to flow mainly towards the Malawi Lake.

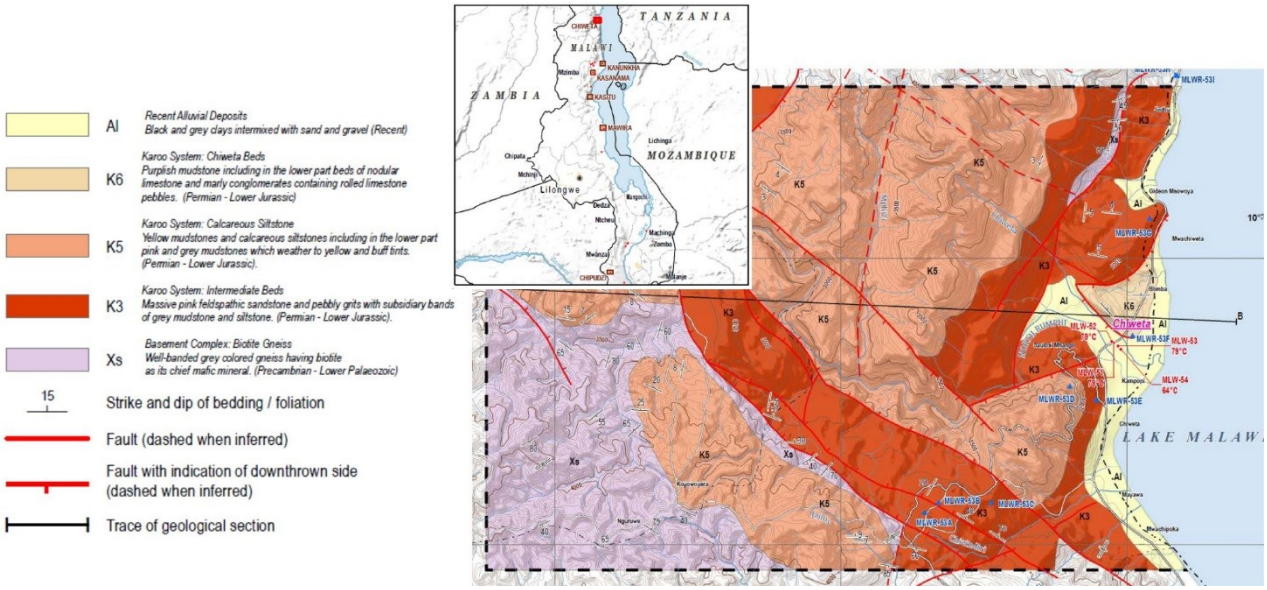

Figure 1: Geological and structural map of the Chiweta area.

2. GEOPHYSICAL INVESTIGATIONS AND METHODS

The geophysical survey, together with the geological and geochemical surveys, was carried out in 2017. The area covered by geophysical investigations was about 30 km^2.

2.1 The Magnetotelluric and TEM survey

The Magnetotelluric (MT) and TEM survey has been carried out by means of 60 MT/TEM stations. Their locations are shown in Figure 2. The TEM locations were chosen in order to keep the distance from the corresponding MT sites as short as possible.

Electric and magnetic time series were acquired in the 1000-0.0001 Hz range by means of three broadband Phoenix V5 System. MT data were always acquired simultaneously with a remote reference site (ASM or KWM, Fig. 2).

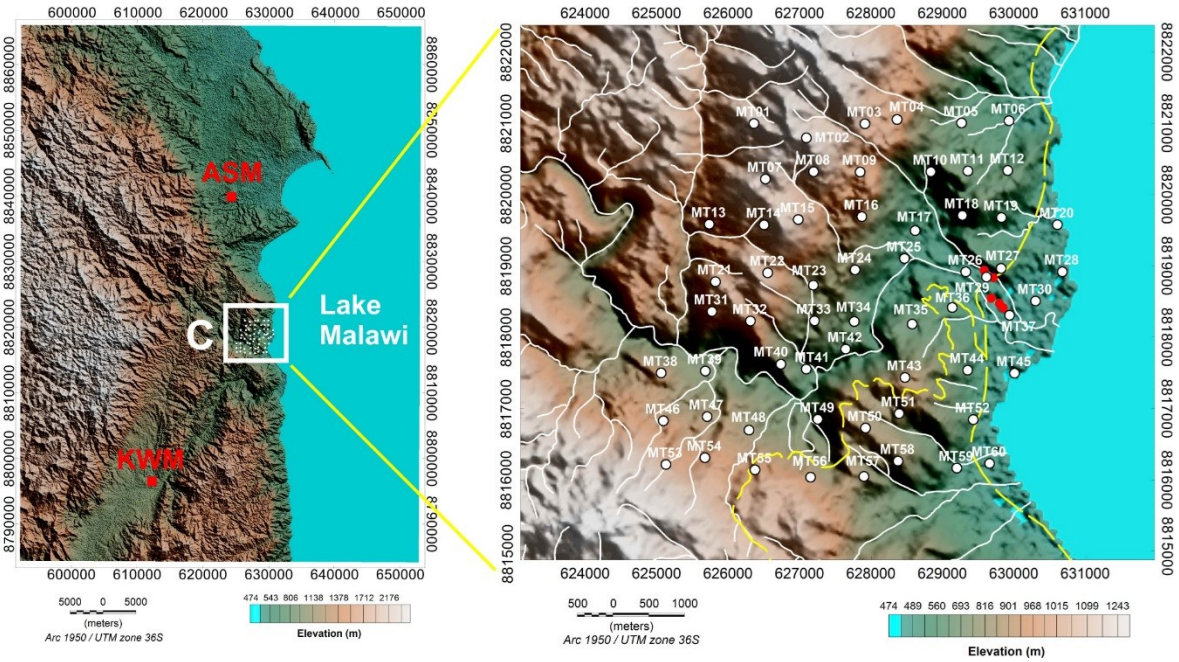

Figure 2: Location of the Chiweta MT survey area. C: Chiweta area (marked by a white rectangle). White dots mark the MT/TEM station locations. The Asimwela and Kawembe MT reference sites are labelled "ASM" and "KWM", respectively (red squares). The Chiweta hot springs are marked by red dots.

MT data have been processed by a combination of different approaches described in MT literature. They have been applied by means of ad hoc programs implemented in the Matlab® environment at the Genoa University. These methods allow to progressively refine the MT data processing and impedance estimation. The five-channel MT data are initially resampled (decimation) and Fast Fourier Transform (FFT) is applied to the 512-samples events extracted from the decimated time series. According to the frequency being analyzed after the FFT, the time series were resampled with frequencies up to 1/8th of the original sample rate, allowing to estimate the MT impedance up to 0.001Hz. After these preliminary steps, we adopted the following workflow: i) Impedance estimation by Remote Reference Least Squares and Robust methods (Sutarno, 2008). ii) Event automatic selection by coherence criteria (Jones and Jodicke, 1984) and impedance estimation from the selected events. iii) Time series inspection and data rejection. iv) Noise analysis and manual exclusion of events and impedance re-estimation from the selected events.

Steps 2-4 are optional: they have been performed when data quality required a deeper intervention on signal. Moreover, for most of the stations steps 3-4 were not necessary. An example of MT data resulting from this processing workflow is given in Figure 3 for station MT22.

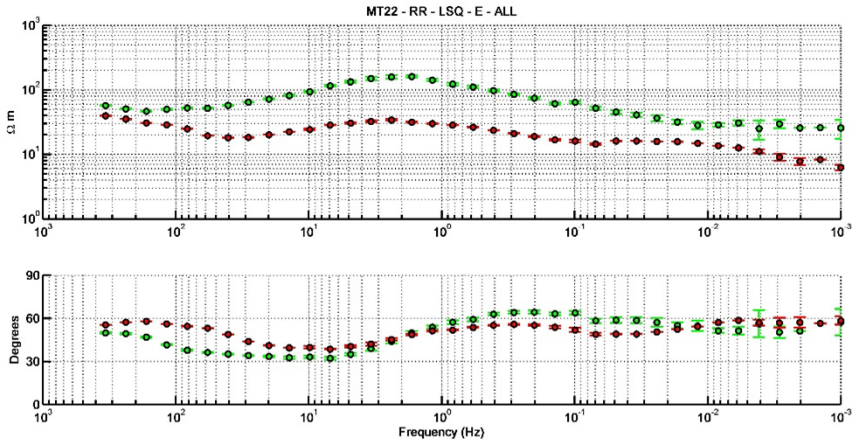

Figure 3: MT xy and yx curves of the station MT22.Green dots indicate the xy-data, while red dots mark the yx ones.

The MT static shift was corrected by means of joint inversion of MT phase and TDEM apparent resistivity data, providing the two apparent resistivity correcting factors (s_{xy}, s_{yx}) for each station. Joint inversion was carried out by means of the Meju (1996) approach.

We also analyzed the strike and dimensions of the resistivity distribution around the MT sites. We based such analysis mainly upon parameters derived from the impedance phase (MT phase tensor, Caldwell, 2004) and geomagnetic tipper (induction arrows, see e.g. Schmucker, 1970). We stress that dimensionality is frequency dependent, since the EM field investigate different portions of earth as a function of the frequency (see e.g. Simpson and Bahr, 2005).

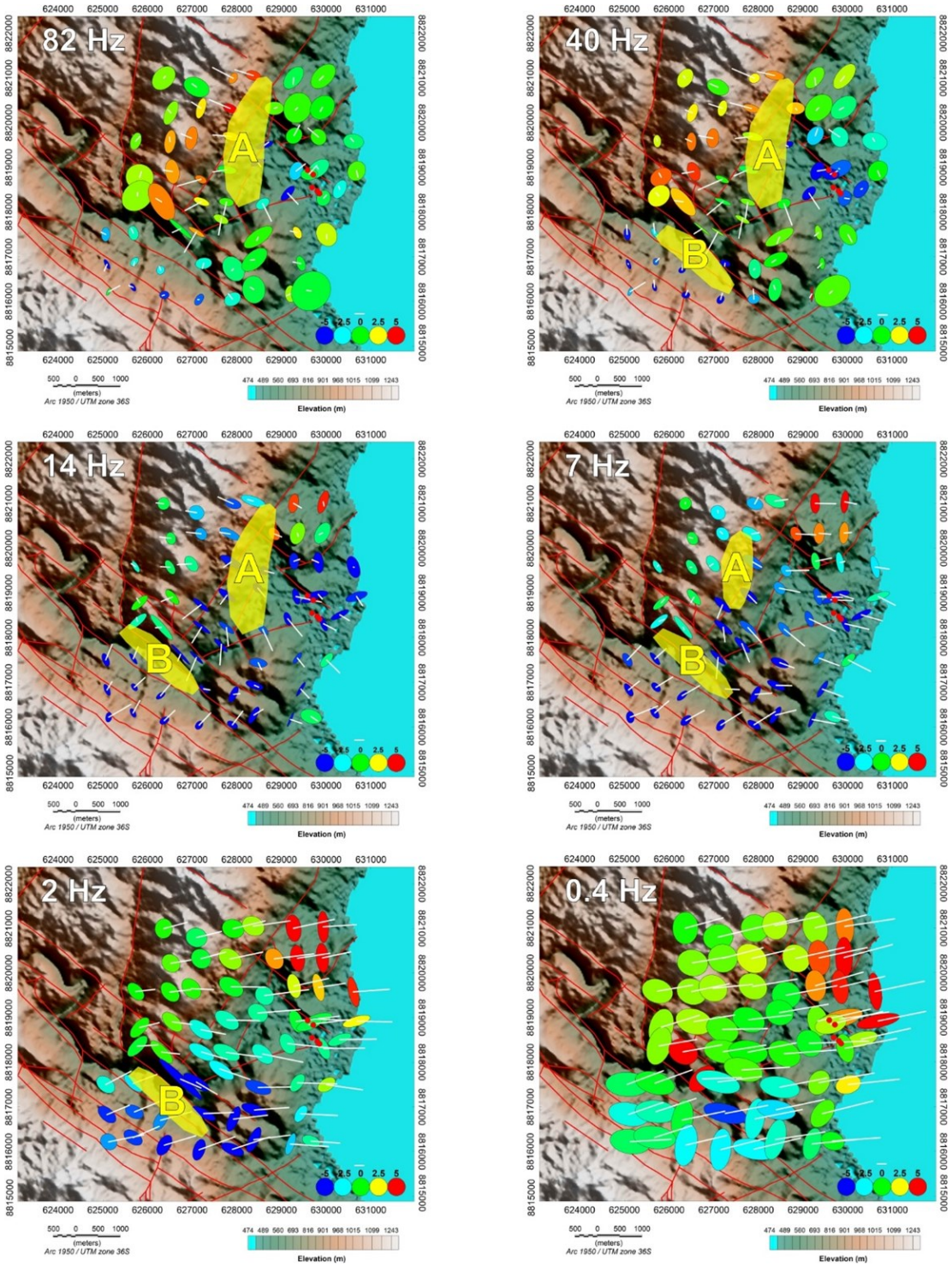

Figure 4: Induction vectors (Parkinson convention) and phase tensor ellipses at the frequencies 82, 40, 14, 7, 2 and 0.4 Hz. The corresponding skin depths for a 100 Ohm m half-space are: 0.55, 0.8, 1.3, 1.9, 3.6 and 8 km. Color scale indicates the phase tensor skew, ranging from -5 (blue) to +5 (red). Note that in the Parkinson convention the induction arrow points towards current concentration, i.e. indicates conductors close to the station. Red capitals labels indicate remarkable areas. Zone A: likely presence of a resistive zone. Zone B: the vectors point to this area. Please note that a few ellipses and induction arrow have been omitted for safe of clarity, since their size was excessive.

Maps of the induction arrows (Parkinson convention, Parkinson, 1959) and phase tensor ellipses are shown in Fig. 4 for the frequencies of 82, 40, 14, 7, 2 and 0.4 Hz. Considering an average resistivity of 100 Ohm m, the corresponding skin depths range between about 550 m and 8 km, thus including in theory every structure of geothermal interest. For frequencies above 14 Hz (corresponding to a skin depth of about 1.3 km), low ellipticity, skew values and short IA are observed all across the area, and a greater variability in the induction arrows is observable. This variability is plausibly enhanced by the limited skin depth, leading MT to sample a local resistivity distribution. Induction arrows become more coherent and longer from 2 Hz: below this frequency, all the IA point toward ENE, thus indicating a NNW EM strike. This direction is in agreement with the main direction of the Nyasa Rift.

While one-dimensional inversion provided a first good approximation of the subsurface resistivity structure, we performed 3-D inversion for interpretation. The inversion has been carried out by means of the ModEM software, a FD software designed for parallel computing (Meqbel, 2009; Egbert and Kelbert, 2012; Kelbert et al., 2014). We used the full (unrotated) and static shift - corrected impedance tensor (Z), jointly with Tz from the whole dataset, using 19 periods in the range between 0.003 s and 1,000 s.

The grid (Fig. 5) consists of 60 X 61 cells in x - and y - directions, extending from -247 to +247 km both S-N (x) and and from -250 to +250 km E-W (y) direction. In the central portion, where the MT sites are located, the horizontal cell size is 300 m. The cell size increases towards the edges of the model (Fig. 10), from 390 to 57015 m. To consider the EM effect on the data of the Lake its bathymetry has been retrieved by digitizing the isobate map of Scholz et al. (2006) and included in the model. According to Halfman (1993) the water resistivity has been set to 40 Ohm m, and of course it has been kept constant during the inversion. In the vertical (z) direction, the grid consists of 72 layers and the bottom of the grid is located at a depth of about 875 km. At shallow depth, the minimum thickness of each cell is 40 m, and then the grid spacing augments logarithmically with depth.

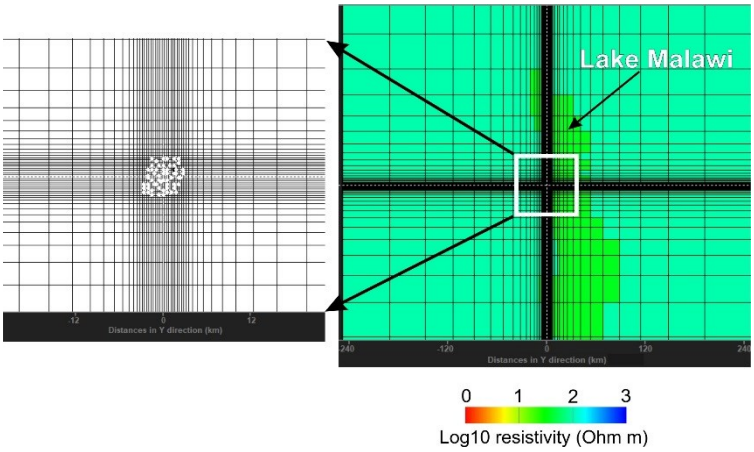

Figure 5: The horizontal grid used. Right: the whole grid, showing Lake Malawi as well. Left: particular of the grid in the survey area. Site locations are marked by white dots.

2.2 The Gravimetric survey

The gravimetric survey survey area was designed to cover the Chiweta geothermal area according to the layout shown in Figure 6. The survey consists of 95 gravity stations on a detailed grid over the focus area arranged over a rectangular grid with nominal station inter-spacing of 0.8 km (Figure 2-4), with a 60 m tolerance from the ideal position. Note that not all gravity stations could be surveyed within the radius of 60 m from the ideal grid station location because of difficult access (thick bush, water, muskeg and/or poor satellite coverage). We used the G927 LaCoste & Romberg gravity meter equipped with electronic beam, electronic pendulum type levels and electronic zero nulling system. For precise vertical location of the measurement points we used a GNSS (Global Navigation Satellite System) differential static measurement system for referencing of the measurement location, with one unit used as base acquiring continuously and one unit used as rover moving along the gravity points.

We applied standard corrections to the measured gravity. The Bouguer (plate) and Terrain Corrections both assume a uniform normal reference density to be estimated. In our case the Karoo sediments outcrop over the survey area (see Fig. 1). Since no direct density measurements are available, we used the Parasnis (1951) approach to infer the reference density. The obtained density value (2640 kg/cm) is in good accordance with the values reported in the literature for the Karoo sediments (Baiyegunhi et al., 2014), that are mainly made by sandstones.

After standard corrections we obtained the Bouguer anomaly map. The final residual Bouguer anomaly map has been obtained as high pass filtering of the Bouguer anomaly with a Butterworth high pass filter of order 8 and cutoff wavelength of 9 km. The result is shown in Figure 7.

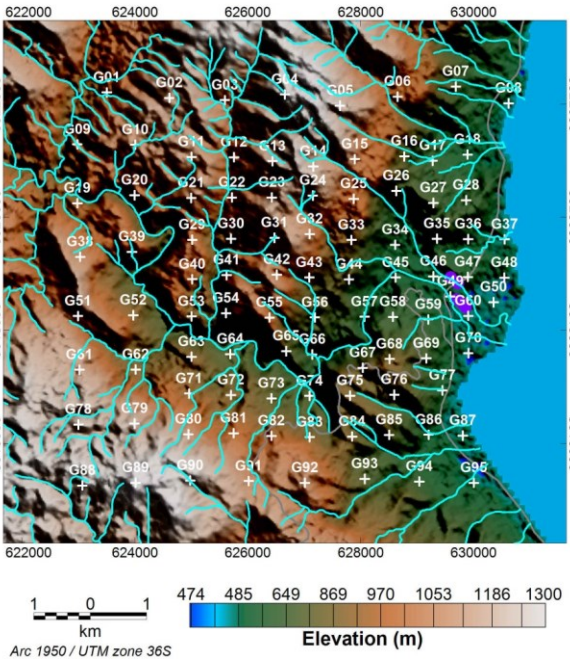

Figure 6: Location (white crosses) of the 95 survey gravity stations (G001-G095). Purple circles: thermal manifestations. Cyan and grey: rivers and main roads.

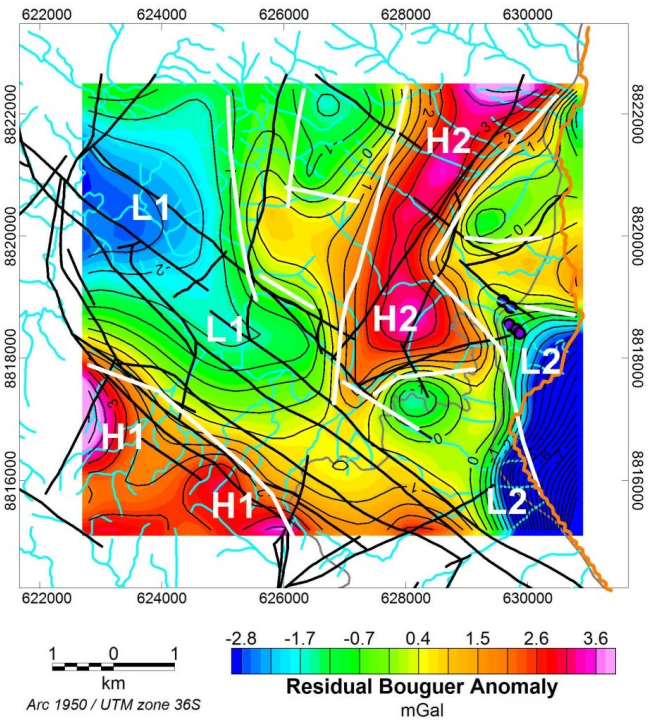

Figure 7: Residual Bouguer Anomaly map (colour grid and contour lines). White lines: gravimetric lineaments derived from the horizontal gradient of the residual Bouguer anomaly. Black lines: lineaments derived from the remote sensing analysis. Purple circles: hot springs. Cyan and grey lines: main rivers and roads respectively.

The anomalies that can be identified in the map are: i) anomaly high H1: it is located in the SW sector of the area with trend NW-SE; ii) anomaly high H2: it is located in the NE sector; it has a linear pattern trending N to NNE; iii) anomaly highs H3 and H4: limited in size, they border the anomaly stripe H2; iv) anomaly low L1: it is located in the NW sector and shows the same NW-SE trend as H1; v) anomaly low L2: it is located at the border of the survey area in the SE sector; the anomaly values are the lowest, the trend is NE-SW.

We have estimated the depth of the sources via the Spector and Grant (1970) method. The radially averaged power spectrum (Figure 8, upper panel) is computed and plotted in logarithmic scale against the wavenumber. The mean depth of the sources is proportional to the slope of the spectrum. The main anomalies in the map have wavelength in the range 0.7-3 km that corresponds to a wavenumber in the range 0.3-1.5 1/km. Therefore, the estimated mean depth of the sources is approximatively 0.2-1 km (Figure 8, lower panel).

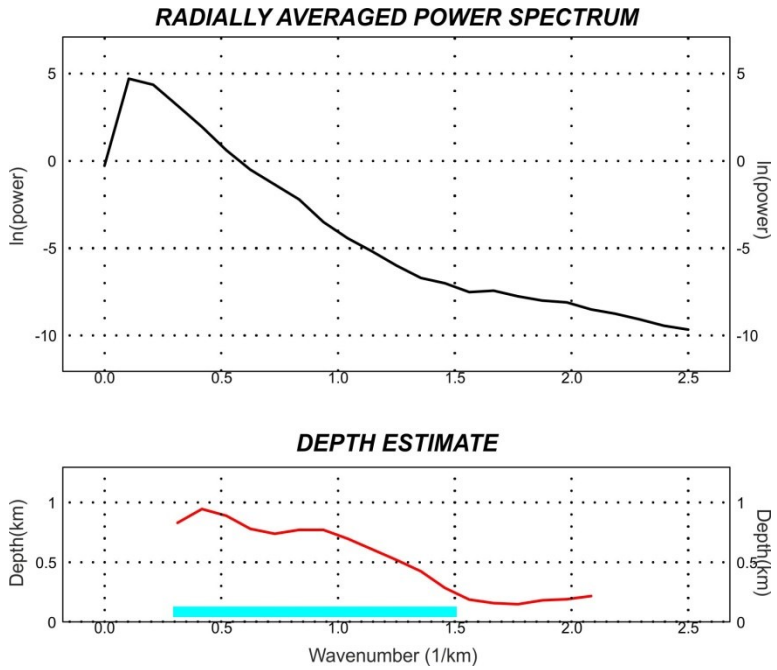

Figure 8: Depth estimation by the radially averaged power spectrum method of Spector and Grant. The transversal wavenumber of the elongated NE-SW gravimetric anomaly is in the range 0.3 – 1.5 1/km (in cyan) that implies a mean depth of the sources of about 0.2 – 1 km.

We applied both 2D and 3D inversion to gravimetric data using different stabilizing functionals to improve focusing of the solutions following the approach of Armadillo et al. (2018). Acar and Vogel (1994) introduced the modified total variation stabilizing functional (modTV):

$$s(m) = \int_V \sqrt{|\nabla m(r)|^2 + \beta^2}\, dv$$

This functional does not penalize discontinuity in the model parameters m and allow for piecewise smooth solutions (Vogel and Oman, 1998). The penalties are applied to gradient terms much larger than β while gradient terms much smaller than β are not penalized. For this reason, the resulting models maybe still too smooth to image complex blocky structures.

To reduce the smoothing effect of modTV, Portniaguine and Zhdanov (1999) introduced the minimum gradient support functional (MGS) that would minimize the area where significant variations of the model parameters and/or discontinuity occur:

$$s(m) = \int_V \frac{\nabla m \cdot \nabla m}{\nabla m \cdot \nabla m + \beta^2} dv$$

For a given value of β, the gradient terms that are much less than β have a very small contribution on the total value of s(m), while terms much larger than β have all contributions equal to one and therefore large gradient are not penalized. With this functional, solutions with sharp boundaries are promoted and the penalty for large gradients is reduced (Portniaguine and Zhdanov, 1999).

We have implemented these functionals in a gravimetric data inversion algorithm developed in the MatLab environment. For the gravity forward modelling routine, we have used the formula for 3D prismatic bodies of Banerjee and Das Gupta (1977). The optimization algorithm is based on the Sequential Quadratic Programming (SQP) method (e.g. Nocedal and Wright, 2006) for non-linear inversion problems.

3. RESULTS

3.1 Magnetotelluric 3D models

Here we show our preferred 3D model by means of a) horizontal slices and b) resistivity cross-sections. The horizontal resistivity slices are shown in Fig. 9. In each map we have introduced different information and symbols, namely, the main conductivity anomalies have been labelled by "CA" and the hypothesized faults are marked by white dashed lines.

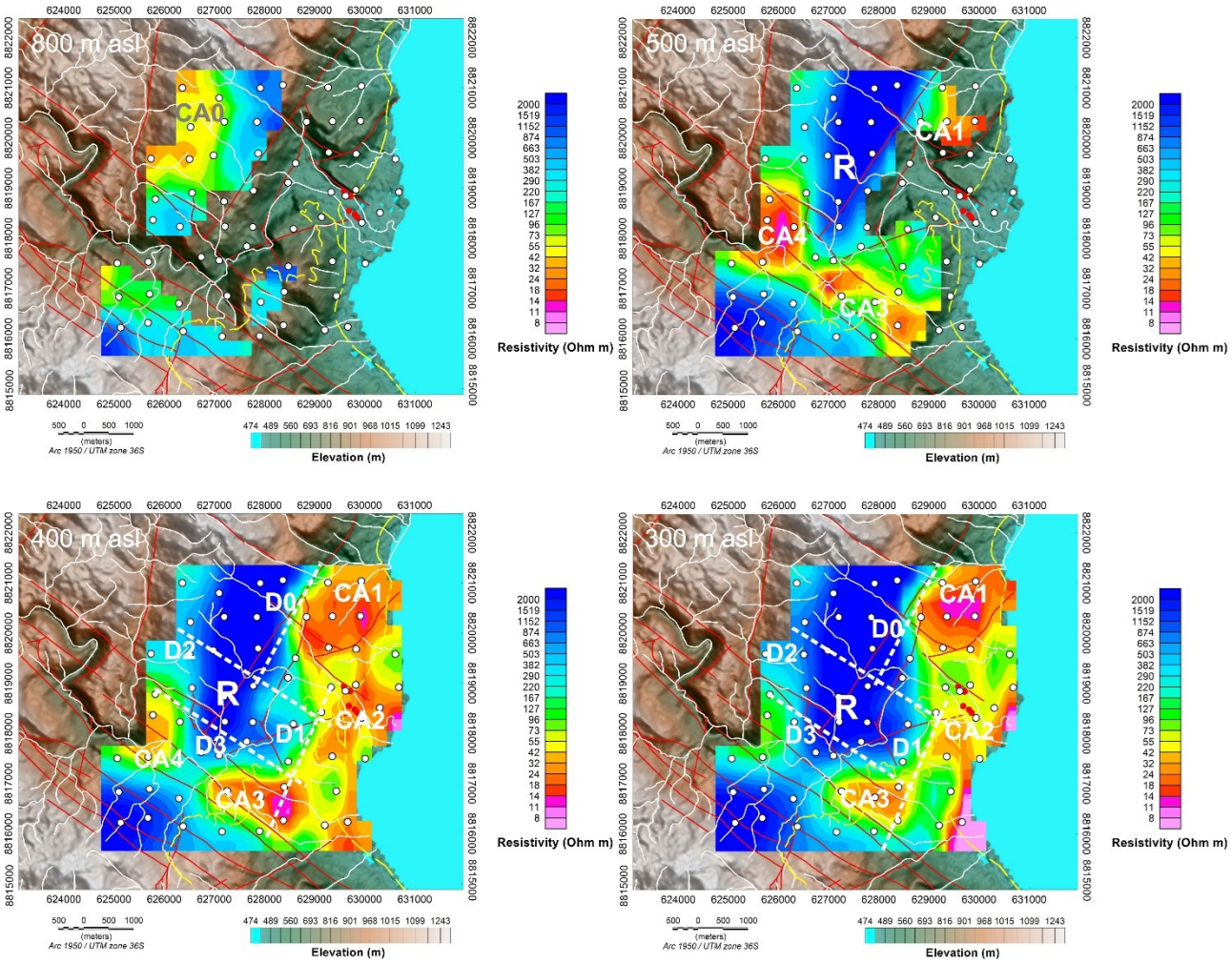

Figure 9a. Horizontal resistivity slices of the 3D model from 800 m a.s.l. to 300 m a.s.l. White dots: MT stations. Red dots: Chiweta hot springs. The main resistivity features are labelled "CA0","CA1" ,"CA2", "CA3", "CA4". White dashed lines indicate the hypothesized lineaments ("D0", "D1","D2", "D3"). The thin red lines mark the lineaments inferred from remote sensing. White thin lines indicate the main rivers.

Observing Fig.9, the following considerations can be made:

- The overall resistivity pattern is characterised by a resistive core (R) centred on the main ridge, surrounded by more conductive areas. This becomes clear below 500 m a.s.l.

- On the western side of the area, on the graben ridge, a relatively conductive anomaly (CA0) is visible. Its resistivity is between about 30 and 50 Ohm m.

- The shoreline is characterised by the presence of a 30-50 Ohm m band (about 1.5 km wide) that could be due to the lake water intrusion; its fading at depth and the resistivity values seem to suggest this hypothesis. We remark that according to Halfman (1993) the resistivity of Lake Malawi is about 40 Ohm m.

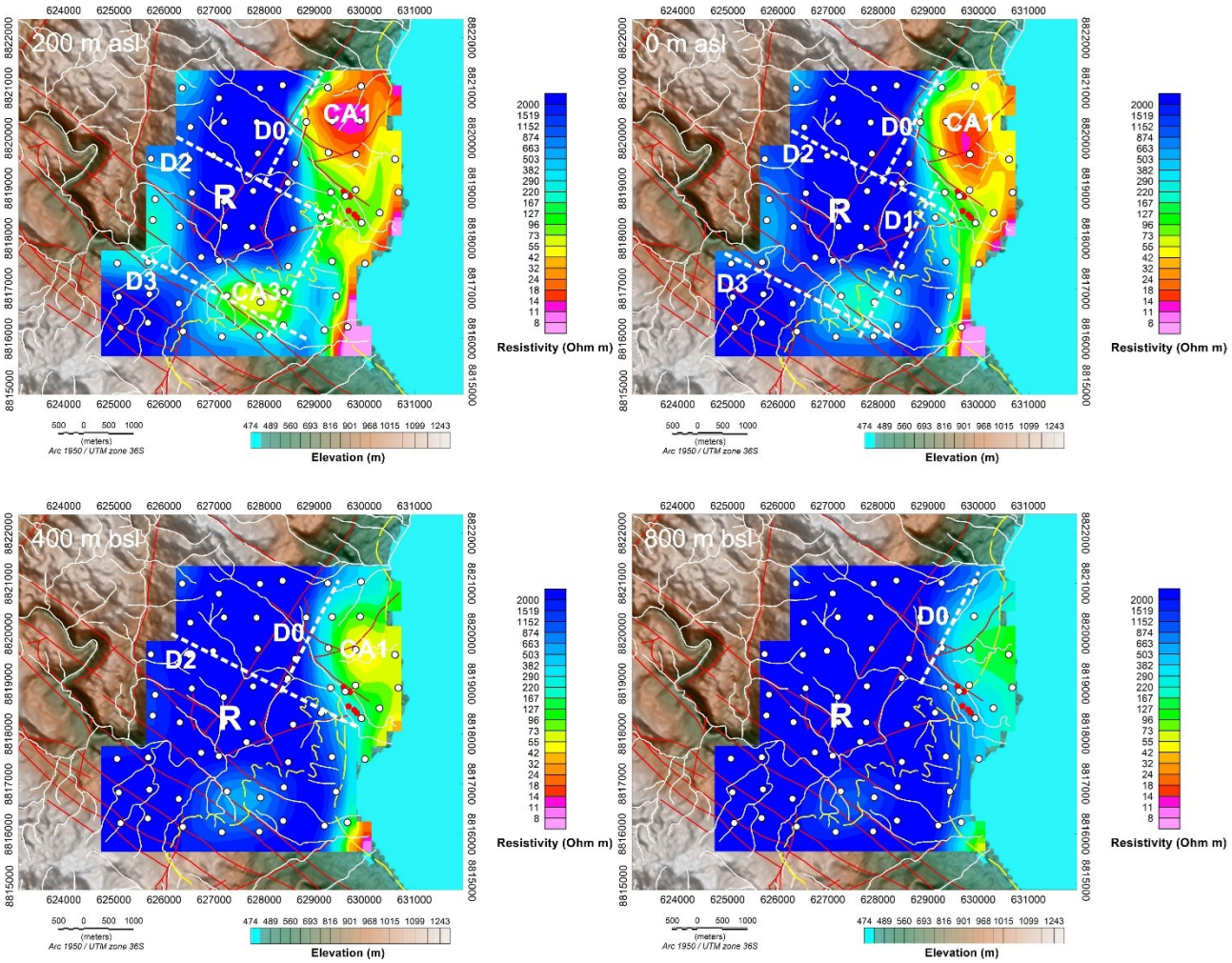

Figure 9b: Horizontal resistivity slices of the 3D model from 200 m a.s.l. to 800 m b.s.l. For symbol description refer to Fig. 9a.

However, despite this ambiguity, some enhanced conductivity zones can be identified (the conductive feature at the south eastern corner of the area is not discussed since it is not adequately sampled):

i. CA1, visible from 500 m a.s.l. (corresponding to elevation greater than the lake altitude) down to 400m b.s.l., and showing a resistivity comprised between about 10 and 30 Ohm m;

ii. CA2, visible between 400 m a.s.l. and 300 m a.s.l. showing a resistivity comprised between about 10 and 30 Ohm m. This anomaly seems to be associated with the hot springs;

iii. CA3, visible between 500 m a.s.l. and 200 m a.s.l., showing a resistivity comprised between about 10 and 20 Ohm m, and CA4, visible between 500 m a.s.l. and 400 m a.s.l., with a resistivity comprised between 10 and 50 Ohm m. It can be furthermore noticed that, given their shape and position, C3 and C4 could be associated with the recognized NW-SE fault zone (see the red lines).

• At great depth (800 m b.s.l.) the resistivity pattern is dominated by the bedrock, plausibly represented by the Gneiss Basement Complex, with values greater than 2000 Ohm m.

• Two families of discontinuities can be hypothesized:

i. a NE-SW family (D0-D1)

ii. a NW-SE family (D2-D3)

It can be noticed that the hot springs are located near to the intersection of lineaments D1 and D2.

In Fig. 10 we show the MT resistivity sections extracted from the 3D model along the profiles reported in the inset for each line.

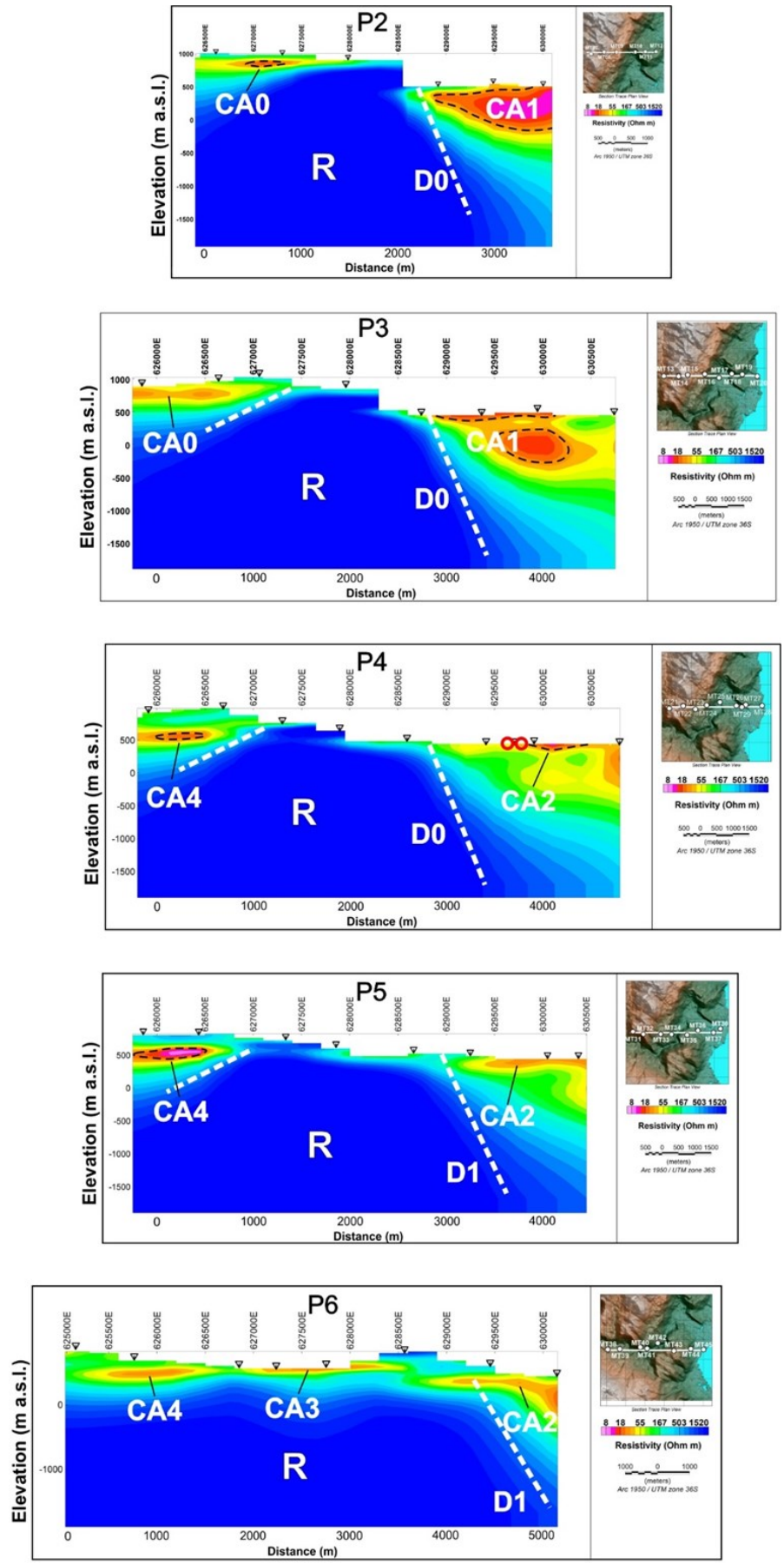

Figure 10: Resistivity sections. The red circles in P4 indicate the location of the Chiweta hot springs. Inverted triangles at surface indicate the MT station locations along the profile. Location of the profile is reported in the inset for each line

In the profiles, the dashed black line marks the smooth version of the 30 Ohm m isoresistive contour, drawn whenever possible for graphical reasons.

The main observations are:

- CA0 is about 200 m thick (considering the 50 Ohm m hypothetical isoresistive contour line), and likely affects the Karoo Calcareous Siltstone and Intermediate Beds.

- CA1 is the thickest anomaly (up to about 750 m along P3, considering the 30 Ohm m contour line). According to the geological map (see Fig. 1), it could also affect the Gneiss Basement Complex, besides the above Karoo Calcareous Siltstone and Intermediate Beds. Its low resistivity (10 Ohm m) could be compatible with the presence of low-T geothermal alteration minerals.

- CA2 is very shallow and thin and lies close to the Chiweta hot springs. However, as can be noticed from Fig. 8a, it lies in the Rumphi River mouth area. Its interpretation is not straightforward, since the showed low resistivity could be then due to low-T alteration in the Karoo Calcareous Siltstone and/or to clayey sediments in this area.

- CA3 and CA4 are thin layers (100-150 m thick) likely affecting the Karoo Calcareous Siltstone and Intermediate Beds at shallow depths. The resistivity shown by CA4 (about 10 Ohm m) could be explained by low-T alteration in these rocks.

- The discontinuity D0 and D1 are compatible with high-angle normal faults relevant to the Lake Malawi Rift.

Another lineament, plunging toward W, can be hypothesised in profiles P2-P5. It has been marked as a dashed white line without any label.

3.2 Gravimetric focused 2D and 3D models

From the geological map (Fig. 1) it results that the expected main lithologies in the survey area are

i) The Karoo sediments, made by continental clastic sediments (mostly sandstone) with subordinate conglomerate, marls, shales, mudstones and limestones. The mean density of the Karoo sediments has been estimated via the Parasnis approach to be 264 kg/m^3. Local variations are expected since the density of the different sedimentary rocks in the Karoo sediments may range from about 2.7 g/cm^3 for the sandstones to about 2.2 g/cm^3 for the mudstones (e.g. Marè, 2012).

ii) The Basement complex made prevalently by biotite gneisses associated with quartzite, granulite, gabbro, granites, cataclasites. We have assumed a density of 2.84 g/cm3, that is a density contrast of +0.2 g/cm^3 with respect to the Karoo sediments.

The anomalies visible in the residual Bouguer anomaly are likely due to depth variations of the basement complex. However, second order local density variations in the Karoo sediments and/or in the basement cannot be excluded. In modelling, we have assumed that:

i) The gravimetric highs are due to structural rise of the basement complex (in light blue in figure 11).

ii) The gravimetric lows are associated with structural lows of the basement complex, filled by the Karoo sediments (in light brown in figure 11) with negative density contrast of 200 kg/m^3.

iii) The gravimetric signal can be explained by a simple two densities layer configuration, without taking into account any lithological differentiations in the Karoo sediments and in the complex basement;

Both 2D and 3D inversions have been therefore based on a simple two layers model made by the Karoo sediments overlaying the basement complex with a fixed density contrast of 200 kg/m^3.

The 2D inversion results obtained by the MSG focusing functional are shown in Figure 11. Some general observations about the 2D models are reported in the following:

i) The high residual Bouguer values are associated with horst-like structures in the denser (+200 kg/m^3) complex basement.

ii) The low residual Bouguer values are associated with lower density Karoo sediments filling the graben-like structures in the complex basement.

iii) The resistivity distribution derived from the 3D MT model is well correlated with the density variations in the West sector of both sections P1 and P2. To the East, close to lake Malawi, the resistivity in the Karoo sediments and in the complex basement are considerably lower, suggesting higher alteration

iv) The depth estimations by the Spector and Grant method (see Figure 7) agree with the depth of the inverted basement surface

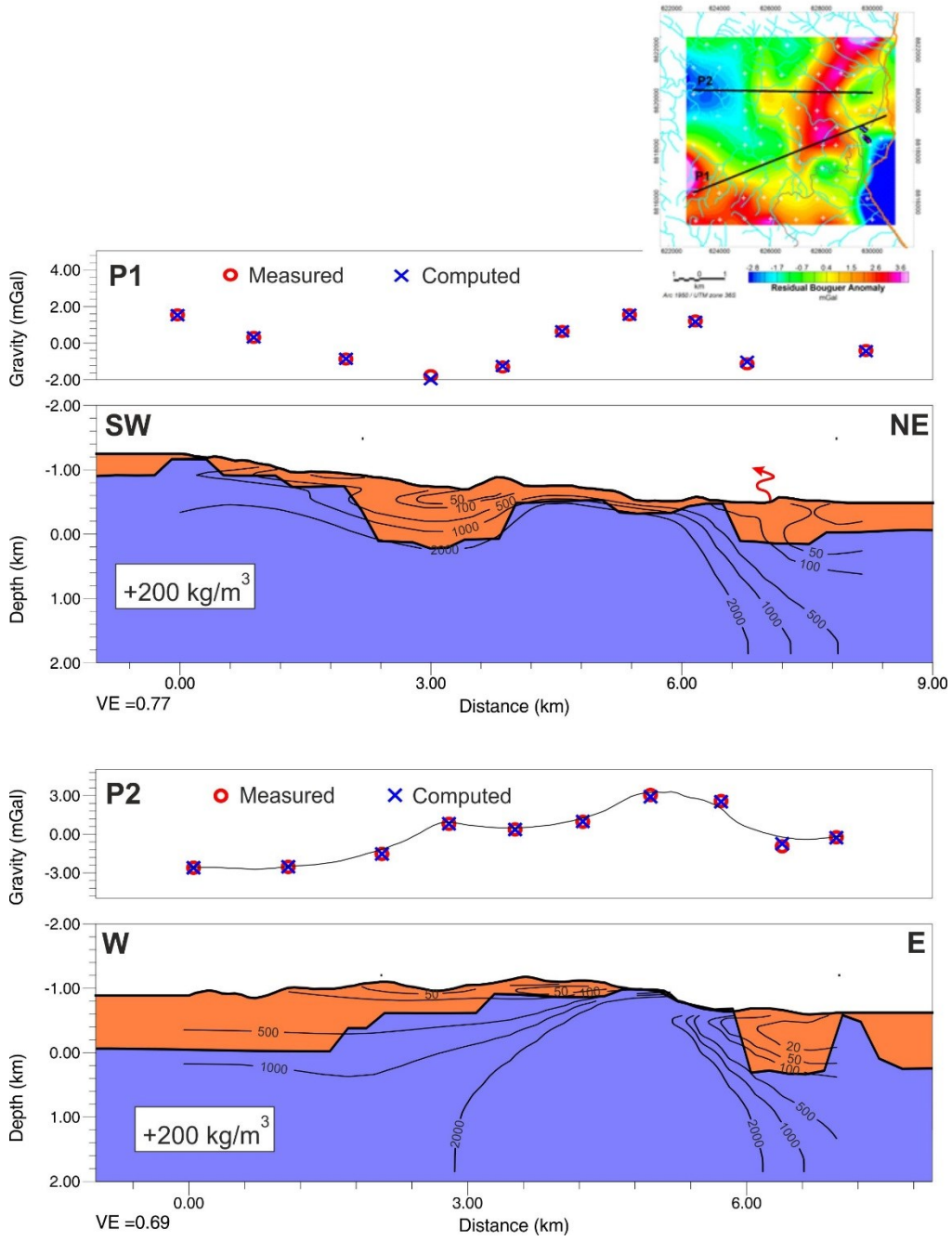

Figure 11: 2D gravimetric focused modelling of the residual Bouguer anomaly along profiles P1 and P2. Upper panel: observed gravity vs calculated gravity. Lower panel: 2D density model. The contour lines of the 3D MT resistivity model are superimposed on the density model. Light brown: Karoo sediments with reference density 2640 kg/m^3. Light blue: complex basement with assumed density 2840 kg/m^3. Red arrow: hot springs.

In Figure 12 we show the elevation of the density contrast surface as derived from the 3D inversion. This surface is assumed here to represent the top of the complex basement. In the figure we have traced as white lines the inferred faults affecting the basement. The faults have been imaged following the local maxima of the horizontal gradient of the basement surface, assuming that the strongest elevation variations of the basement are due to faulting. We have also reported in the same figure as black lines the faults inferred from the remote sensing analysis that match the trends and patterns of the basement elevation variations.

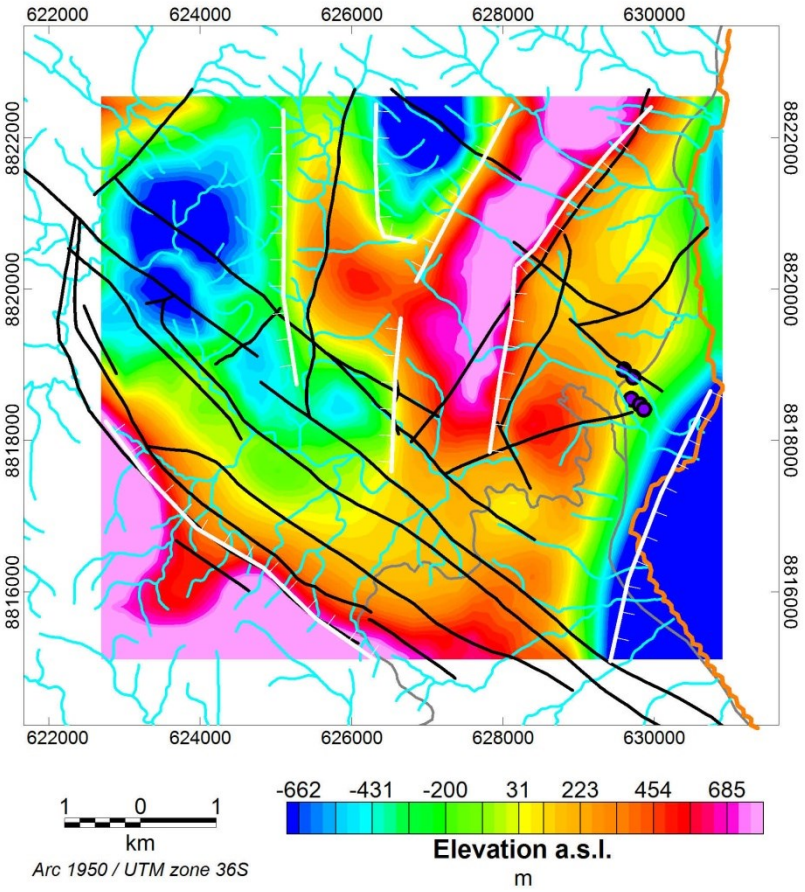

Figure 12: Elevation a.s.l. of the estimated top surface of the complex basement derived from the 3D inversion of gravimetric data. White lines: inferred faults traced along the maxima of the horizontal gradient of the basement surface. Black lines: subset of the lineaments derived from the remote sensing analysis that show good correlation with the strongest elevation variations of the basement surface. Purple circles: hot springs. Cyan and grey lines: main rivers and roads respectively.

The estimated top of the basement is well correlated with the electrical resistivity distribution derived from the 3D MT model. In Figure 13 we show the electrical resistivity slice at 400 m a.s.l. superimposed on the 400 m contour line of the elevation of the estimated top of the basement. This suggest that generally the very high resistivity values (order of magnitude > 1000 Ohm m) of the 3D resistivity model are correlated with the basement rocks. Lower resistivity values may be associated with the Karoo sediments and/or altered basements. Very low resistivity values may be associated with very altered Karoo sediments and/or basement.

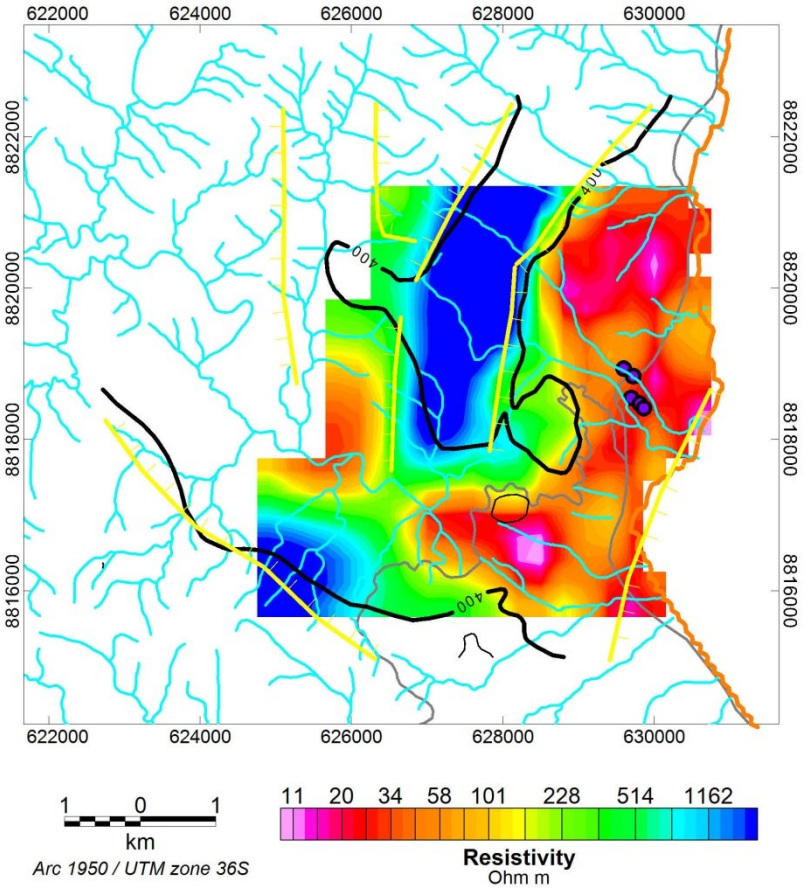

Figure 13: Electrical resistivity slice (colour grid) at 400 m a.s.l. compared with the elevation a.s.l. of the gravimetric basement (400 m contour line). Yellow lines: inferred faults traced along the maxima of the horizontal gradient of the basement surface. Purple circles: hot springs. Cyan and grey lines: main rivers and roads respectively.

4. CONCLUSIONS

The residual Bouguer anomaly map revealed two positive anomalies trending NW-SE and NE-SW respectively. Spector and Grant method indicates a range depth of the sources between 0.2 -1 km. The anomalies can be explained by a simple two layers model that is compatible with the geological evidences. The upper layer is identified with the Karoo sediments, the lower layer with the complex basement (assumed density contrast of +200 kg/m^3 between the two). Focused inverse 2D/3D modelling allows to image the basement surface elevation. The surface shows a horst-graben structure with main trends NW-SE and NE-SW. Sharp elevation variations in the basement are associated with main faults that can be traced on the maps. Of course, the imaged basement top surface must be considered a first order approximation of the true one since it can be biased by lateral density variations in the Karoo and/or in the basement.

The estimated top of the basement is well correlated with the electrical resistivity distribution derived from the 3D MT model. Generally, the very high resistivity values (order of magnitude > 1000 Ohm m) of the 3D resistivity inverse model are correlated with the basement rocks.

A good overview of the overall resistivity structures in the Chiweta area can be obtained looking at the 800, 500 and 400 m a.s.l. resistivity slices from the preferred 3D model (Fig. 12a). From these slices is possible to identify several zones of anomalous conductivity and some lineaments as well. A convenient way to summarize all the features discussed in the previous paragraphs is to superimpose them on the geological map, as shown in Fig.14. In this figure, the recognized faults are also reported. Please note that the shown resistivity features don't necessarily refer to the same depth.

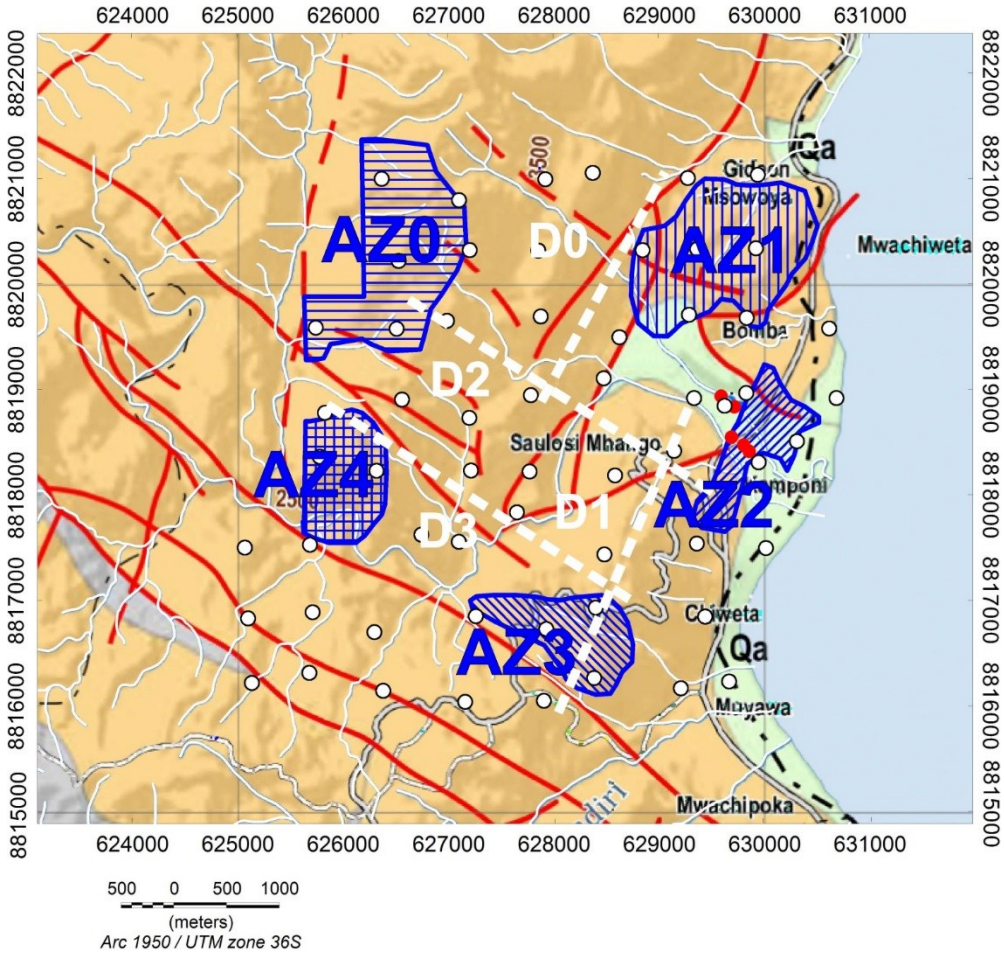

Figure 14: Synthesis map with the main outcomes superimposed on the geological map. Yellow circles: Chiweta hot springs. AZ0, AZ1, AZ2, AZ3, AZ4: alteration zones, marked by different hatches. D1, D2, D3, D4: main lineaments hyphothesised from the 3D resistivity modelling. The lineaments inferred from the remote sensing are marked by red lines. White lines indicate the man rivers. For the geological map legend, please refer to Fig. 1

The AZ0 shown in the figure has been inferred by considering the 50 Ohm m isoresistive contour line identifying the CA0 resistivity anomaly well visible in the 800 m a.s.l. slice. This zone could be explained by the presence of high-T alteration minerals, at relatively shallow depths (about 150 m) in the Karoo Calcareous Siltstone and Intermediate Beds.

The AZ1 has been identified by considering the 30 Ohm m isoresistive line contouring the corresponding CA1 anomaly visible in the 400 m a.s.l. slice. This anomaly is characterised by resistivity values low as 10 Ohm m, that suggest the presence of low-T alteration minerals. Given its thickness, it could affect also the Gneiss Basement Complex, in addition to the shallower Karoo Calcareous Siltstone and Intermediate Beds.

The AZ2 has been inferred by considering the 30 Ohm m isoresistive contour line identifying the corresponding CA2 resistivity anomaly visible in the 400 m a.s.l. slice. This anomaly is characterised by resistivity values low as 10 Ohm m. However, given the presence of the Rumphi River alluvial sediments, its low resistivity could be alternatively explained by the presence of fine-grained or clayey materials and /or to low-T alteration in the Karoo Calcareous Siltstone.

The AZ3 and AZ4 zones affect at shallow depths the Karoo Calcareous Siltstone and Intermediate Beds. For AZ4, given its low resistivity (10 Ohm m), a possible explanation could be low-T alteration.

Two families of lineaments have been inferred, n good agreement with the gravimetric ones: one NE-SW trending (D0 and D1) and one the NW-SE (D2, D3). It can be noticed that the hot springs are located near to the intersection of D1 and D2, suggesting for a geothermal origin of the AZ2 alteration zone.

AKNOWLEDGEMENTS

This work was funded by the Icelandic International Development Agency (ICEIDA) and the Nordic Development Fund (NDF). The Tanzania Geothermal Development Company (TGDC), ELC-Electroconsult S.p.A., Tellus s.a.s. and the Department of Earth, Environment and Life Sciences (DISTAV) of the University of Genoa provided instrumental and technical support.

REFERENCES

Acar, R., and Vogel, C. R. “Analysis of total variation penalty methods” Inverse Problems, 10, 1217-1 229 (1994).

Baiyegunhi C., T.L. Oloniniyi, and O. Gwavava, 2014. The correlation of dry density and porosity of some rocks from the Karoo Supergroup: A case study of selected rock types between Grahamstown and Queenstown in the Eastern Cape Province, South Africa. IOSR Journal of Engineering, Vol. 04, Issue 12, PP 30-40

Banerjee, B., and Das Gupta, S. P. “Gravitational attraction of a rectangular parallelepiped”. Geophysics, 42 (5), 1053-1055 (1977).

Caldwell T.G., Bibby H.M., Caldwell C. (2004). The magnetotelluric phase tensor. Geophys. J. Int., 158,457-469.

Constable, S. C., Parker, R. C., and Constable, G. “Occam's inversion: a practical algorithm for generating smooth models from EM sounding data” Geophysics, 52, 289-300 (1987).

Egbert, G.D. & Kelbert, A. "Computational recipes for electromagnetic inverse problems". Geophys. J. Int.,189(1), (2012), 251-267.

Gamble, T.D., Goubau, W.M., Clarke, J. "Magnetotellurics with a remote magnetic reference". Geophysics, 44, (1979) 53-68.

Jones A.G.and Jodicke H. “Magnetotelluric transfer function estimation improvement by a coherence-based rejection technique”. Paper presented at 54th Annual International Meeting, Soc. of Expl. Geophys., Atlanta, Ga., Dec. 2-6, 1984.

Kelbert A, Meqbel N, Egbert GD, Tandon K. "ModEM: A modular system for inversion of electromagnetic geophysical data". Computers & Geosciences, 66, (2014), 40-53.

Meju, M. "Joint inversion of TEM and distorted MT soundings: some effective practical considerations". Geophysics, 61, (1996) pp. 56-65.

Meqbel, N. "The electrical conductivity structure of the Dead Sea Basin derived from 2D and 3D inversion of magnetotelluric data". PhD thesis, Free University of Berlin, Berlin, Germany, (2009).

Nocedal, J., and Wright, S. J. “Numerical Optimization”, Second Edition. Springer Series in Operations Research, Springer Verlag (2006).

Parasnis D.S. "A study of rock densities in the English Midlands". Roy. Astr. Soc., Geophys. Suppl., 6, (1951),252-71.

Parker R.L. "The Rapid Calculations of Potential Anomalies". Geophys. J. R. Astr. Soc. 31, (1972), 447-455.

Parkinson W.D. (1959). Direction of rapid geomagnetic fluctuations. Geophys. J., vol. 2, pp. 1-14.

Portniaguine, O., and Zhdanov, M. S. “Focusing geophysical inversion images”. Geophysics, 64, 3, 874-887 (1999).

Rudin, L. I., Osher, S., and Fatemi, E. “Nonlinear total variation based noise removal algorithms”, Physica D, 60, 259-268 (1992).

Schmucker U. (1970). Anomalies of geomagnetic variations in the south-western United States. Bull. Scripps Inst. Oceanog. 13, University of California.

Simpson F., Bahr K. (2005). Practical Magnetotellurics. Cambridge University Press, 254 pages.

Spector A, and F.S. Grant. "Statistical models for interpreting aeromagnetic data". Geophysics, vol. 35 (1970) no. 2, 293-302Annex 1 – Field Data and Corrected Values.

Sutarno D. (2008). Constrained robust estimation of magnetotelluric impedance functions based on a bounded-influence regression M-estimator and the Hilbert transform. Nonlin. Processes Geophys., 15, 287-293.

Tikhonov, A. N., and Arsenin, V. Y. “Solution of ill-posed problems” V. H, Winston and Sons (1977).

Vogel, C. R., and Oman, M. E. “Fast total variation based reconstruction of noisy blurred images” IEEE Trans. Image Processing., 7, 813-824 (1998).

Zhdanov, M. S. “Geophysical inverse theory and regularization problems”, Methods in Geochemistry and Geophysics, 36, Elsevier (2002).

Zhdanov, M. S., and Keller, G. V. “The Geoelectrical Methods in Geophysical Exploration”. Elsevier (1994).Verma, A., and Pruess, K.: Enhancement of Steam Phase Relative Permeability Due to Phase Transformation Effects in Porous Media, *Proceedings,* 11th Workshop on Geothermal Reservoir Engineering, Stanford University, Stanford, CA (1986). <Reference Style>